

MAY 10 2024

Theoretical and numerical study on transient acoustic wave propagation across ice layers in the Arctic Ocean

Qitian Zeng  ; Shengxing Liu; Liguang Tang  ; Zhenglin Li



J. Acoust. Soc. Am. 155, 3132–3143 (2024)

<https://doi.org/10.1121/10.0025982>





WE BRING THE NOISE,
YOU BRING THE PRODUCTS

COMMITTED TO A SMARTER,
MORE CONNECTED FUTURE

 ETS-LINDGREN
An ESCO Technologies Company

Theoretical and numerical study on transient acoustic wave propagation across ice layers in the Arctic Ocean

Qitian Zeng,¹  Shengxing Liu,^{1,2,a)} Liguang Tang,^{1,3}  and Zhenglin Li^{2,4,5}

¹Key Laboratory of Underwater Acoustic Communication and Marine Information Technology (Ministry of Education), College of Ocean and Earth Sciences, Xiamen University, Xiamen 361102, China

²Southern Marine Science and Engineering Guangdong Laboratory (Zhuhai), Zhuhai 519000, China

³State Key Laboratory of Acoustics, Institute of Acoustics, Chinese Academy of Sciences, Beijing 100190, China

⁴School of Ocean Engineering and Technology, Sun Yat-sen University, Zhuhai 519000, China

⁵Key Laboratory of Comprehensive Observation of Polar Environment (Sun Yat-sen University), Ministry of Education, Zhuhai 519000, China

ABSTRACT:

The study of transient acoustic wave propagation across the Arctic Ocean ice layer provides theoretical guidance for the design of trans-ice acoustic communication systems. In this study, the Arctic Ocean was modeled as an ice–water composite structure, where the ice and water are regarded as an elastic solid and liquid, respectively. An analytical transient solution for acoustic wave propagation in this structure was derived using the eigenfunction expansion method. Further, the numerical procedures were presented and used to analyze the acoustic wave propagation characteristics across the ice layer. The results show that waveforms corresponding to the radial displacements are more severely distorted than the axial displacements. The amplitudes of the radial and axial displacements decreased rapidly with increasing propagation distance. The ice thickness had a greater impact on the radial displacement than axial displacement; the thicker the ice, the greater the distortion for both radial and axial displacements.

© 2024 Acoustical Society of America. <https://doi.org/10.1121/10.0025982>

(Received 18 November 2023; revised 27 March 2024; accepted 25 April 2024; published online 10 May 2024)

[Editor: D. Benjamin Reeder]

Pages: 3132–3143

I. INTRODUCTION

Studying acoustic wave propagation in the frozen Arctic Ocean is of great importance to the improvement of sonar and could help to establish various long-term acoustic systems for the efficient monitoring of climate and environmental changes in the Arctic. Moreover, acoustic waves provide a means of communication across the ice (Yin *et al.*, 2021). Setting up a geophone on the surface of the ice to detect transient waves can enable the transmission of acoustic signals across the ice layer (Han *et al.*, 2019; Dosso *et al.*, 2002; Dosso *et al.*, 2003; Dosso, 2014). However, the efficacy of communication depends on the propagation properties of acoustic waves; therefore, it is necessary to investigate the characteristics of transient acoustic wave propagation across ice layers in ice–water composite structures.

Many theoretical and experimental studies have been conducted on acoustic wave propagation in the Arctic Ocean since the 1960s. Kutschale (1969) measured long-distance acoustic wave propagation in the center of the Arctic Ocean and explained group-velocity dispersion characteristics using normal-mode theory. Diachok (1976) studied subglacial acoustic propagation loss in the central Arctic Ocean by combining the Burke–Twersky scattering model (Burke and Twersky, 1966) with ray theory. Gavrilov and

Mikhalevsky (2006) experimentally analyzed the effect of the geometric parameters of ice sheets and acoustic velocity profiles on propagation loss in the Arctic Franz Victoria Sea. Hope *et al.* (2017) studied acoustic propagation loss in the Arctic marginal ice zone using the wavenumber integration method and found that the roughness of the ice–water interface was one of the most influential factors. Penhale *et al.* (2018) studied the propagation characteristics of acoustic waves through different media, including air, ice, and underwater, using hammers (acting on the ice surface), cannons (acting on the air), and underwater speakers as excitation sources. They found that the propagation loss between 125 and 2000 Hz varied from approximately 3 to 6 dB per doubling of distance. Alexander *et al.* (2013) simulated acoustic propagation loss under Arctic ice by combining the Bellhop model with a bounce program. Yin *et al.* (2021) conducted a cross-ice acoustic communication experiment and explained why the sound speed of the signal received on the upper surface of the ice was slower than that in the water using normal-mode theory. Reeder *et al.* (2022) conducted an ice-layer resonance experiment in the Arctic Ocean and proposed a method to infer ice thickness through acoustic waves generated by walking on snow-covered ice. Liu *et al.* (2021) analyzed the dispersion characteristics and wave structures of guided waves propagating in an Arctic ice–water coupled system using the wave propagation theory for solids and liquids.

^{a)}Email: liusx@xmu.edu.cn

Trans-ice acoustic communication in the Arctic has become a critical research topic because of its application in marine exploration and exploitation, environmental monitoring, and military operations (Collins and Siegmann, 2021; Li *et al.*, 2021; Chen *et al.*, 2021). Trans-ice communication experiments were conducted in lakes and oceans, yielding valuable results (Dosso *et al.*, 2002; Dosso *et al.*, 2003; Yin *et al.*, 2021). Studying the transient acoustic propagation across ice is important to trans-ice acoustic communication. Although experimental measurement is the most straightforward and effective way to obtain the transient acoustic propagation characteristics, it is challenging and costly to conduct on-site experiments due to the harsh Arctic environment. Furthermore, the geometry and acoustic parameters of the ice layer vary in different regions of the Arctic. Consequently, the data on propagation characteristics measured in one area may not be valid for other areas. Theoretical and numerical methods are alternatives for understanding the transient acoustic propagation characteristics, as they can analyze the transient acoustic propagation characteristics in different ocean areas by setting different parameters with high efficiency.

The aforementioned Arctic acoustic propagation models, such as normal-mode and ray theory, primarily focus on wave propagation in water. They cannot be used to analyze the acoustic propagation characteristics across the ice layer because they typically treat ice sheets as reflectors or scatterers. Therefore, it is necessary to extend these models or develop a new model that can analyze the trans-ice propagation characteristics of acoustic waves. The eigenfunction expansion method (EEM), which uses the eigenfunctions to express a wave function, is widely used to study the transient dynamics responses of elastic solids (Reismann, 1968; Reismann and Pawlik, 1974; Weaver and Pao, 1982; Liu and Qu, 1998; Yin and Yue, 2002; Tang and Xu, 2010; Tang and Wu, 2012; Tang *et al.*, 2012). In the present study, EEM was introduced to investigate transient acoustic wave propagation across the Arctic Ocean ice layer. A concise analytical transient solution to an acoustic wave propagation in an ice–water composite structure was derived. Moreover, the trans-ice propagation characteristics of acoustic waves in the Arctic Ocean were numerically analyzed.

The remainder of this paper is organized as follows: Sect. II introduces the model of acoustic propagation across the ice layer, including the governing equations and boundary conditions. Section III presents the analytical transient solution to acoustic waves propagating in an ice–water composite structure, derived using EEM. Section IV presents the numerical procedures for calculating transient displacements and discusses the numerical results. Finally, Sec. V concludes the paper.

II. STATEMENT OF THE PROBLEM

In this study, the Arctic Ocean was regarded as an ice–water composite structure, as shown in Fig. 1, where the excitation source was placed in the water. An axisymmetric

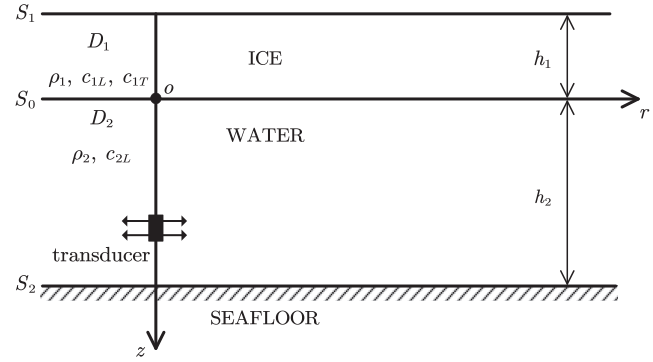


FIG. 1. The Arctic Ocean is modeled as an ice–water composite structure. D_1 is the ice region and D_2 is the water region, with depths of h_1 and h_2 , densities of ρ_1 and ρ_2 , longitudinal wave velocities c_{1L} and c_{2L} , respectively, and transverse wave velocity c_{1T} in the ice region. The upper surface of the ice, lower surface of the water, and ice–water interface are denoted as S_1 , S_2 and S_0 , respectively.

cylindrical coordinate system was used, whose ordinate origin was located at the ice–water interface. A cylindrical transducer was used as the excitation source, the center of which was located at $(0, z_0)$. The external force generated by the transducer was assumed to be radial.

To simplify the analysis, we assumed that ice and water are a homogeneous isotropic elastic solid and fluid, respectively. The region occupied by ice is denoted as

$$D_1 = \{(r, \theta, z; \rho_1, c_{1L}, c_{1T}) | 0 \leq r \leq R, 0 \leq \theta < 2\pi, -h_1 \leq z \leq 0\}, \quad (1)$$

where ρ_1 is the ice density, c_{1L} and c_{1T} are the velocities of the longitudinal and transverse waves in ice, respectively, h_1 is the thickness of the ice, and R is the radius of the composite structure. The region occupied by water is denoted as

$$D_2 = \{(r, \theta, z; \rho_2, c_{2L}) | 0 \leq r \leq R, 0 \leq \theta < 2\pi, 0 < z \leq h_2\}, \quad (2)$$

where ρ_2 and c_{2L} are the density and longitudinal wave velocity corresponding to the water, respectively, and h_2 is the depth of the water. The composite structure region as a whole is denoted as D , that is, $D = D_1 \cup D_2$. The boundary of region D encloses a complete space. We present a theoretical derivation and numerical analysis of the elastodynamic problem in this space for the given boundary constraints.

The vector displacements of a particle in regions D_1 and D_2 are denoted by $\mathbf{u}_1(\mathbf{x}, t)$ and $\mathbf{u}_2(\mathbf{x}, t)$, respectively. They are governed by the following Navier equation:

$$\mathbf{L}_i[\mathbf{u}_i(\mathbf{x}, t)] + \rho_i \mathbf{f}_i(\mathbf{x}, t) = \rho_i \frac{\partial^2 \mathbf{u}_i(\mathbf{x}, t)}{\partial t^2}, \quad \text{in } D_i, \quad i = 1, 2, \quad (3)$$

with the linear differential operators

$$\mathbf{L}_1 = (\lambda_1 + 2\mu_1)\nabla\nabla \cdot - \mu_1\nabla \times \nabla \times \quad (4)$$

and

$$\mathbf{L}_2 = \lambda_2 \nabla \nabla, \quad (5)$$

where $\lambda_1 = \rho_1(c_{1L}^2 - 2c_{1T}^2)$ and $\mu_1 = \rho_1 c_{1T}^2$ are the Lamé constants corresponding to ice, $\lambda_2 = \rho_2 c_{2L}^2$ corresponds to water, and $\mathbf{f}_1(\mathbf{x}, t)$ and $\mathbf{f}_2(\mathbf{x}, t)$ are the body forces imposed on the ice and water regions, respectively.

For a two-dimensional axisymmetric problem, $\mathbf{u}_1(\mathbf{x}, t)$ and $\mathbf{u}_2(\mathbf{x}, t)$ can be linearly expressed in terms of the unit vectors \mathbf{e}_r and \mathbf{e}_z along the coordinate axes r and z , i.e.,

$$\begin{pmatrix} \mathbf{u}_1(\mathbf{x}, t) \\ \mathbf{u}_2(\mathbf{x}, t) \end{pmatrix} = \begin{pmatrix} u_1^r(r, z, t) & u_1^z(r, z, t) \\ u_2^r(r, z, t) & u_2^z(r, z, t) \end{pmatrix} \begin{pmatrix} \mathbf{e}_r \\ \mathbf{e}_z \end{pmatrix}. \quad (6)$$

Assuming that the upper surface of the ice layer satisfies the traction-free boundary condition, the ice–water interface satisfies the normal displacement and stress continuities, the shear stress vanishes at the interface, and the seafloor satisfies the absolute hard boundary condition, i.e., the normal displacement is zero at the seafloor, we have

$$\boldsymbol{\sigma}_1(\mathbf{x}, t) = 0, \quad \text{on } S_1, \quad (7)$$

$$\begin{aligned} \mathbf{u}_1(\mathbf{x}, t) \cdot \mathbf{n} &= \mathbf{u}_2(\mathbf{x}, t) \cdot \mathbf{n}, \quad \boldsymbol{\sigma}_1(\mathbf{x}, t) \cdot \mathbf{n} \\ &= \boldsymbol{\sigma}_2(\mathbf{x}, t) \cdot \mathbf{n}, \quad \sigma_1^z(\mathbf{x}, t) = 0, \quad \text{on } S_0, \end{aligned} \quad (8)$$

$$\mathbf{u}_2(\mathbf{x}, t) \cdot \mathbf{n} = 0, \quad \text{on } S_2, \quad (9)$$

where $\boldsymbol{\sigma}_i$, ($i = 1, 2$) is the stress tensor with $(\sigma_i^{rz}, \sigma_i^{zz})$ components and \mathbf{n} denotes the outward unit normal vector of the corresponding surface. Without loss of generality, the initial state of the system was given by

$$\mathbf{u}_i(\mathbf{x}, 0) = \dot{\mathbf{u}}_i(\mathbf{x}, 0) = 0, \quad i = 1, 2. \quad (10)$$

The analytical solution of the transient acoustic waves in the composite structure can be obtained by solving Eq. (3) under the boundary conditions of Eqs. (7)–(9) and initial condition of Eq. (10).

III. ANALYTICAL SOLUTION FOR TRANSIENT ACOUSTIC WAVES

The orthogonality and completeness of eigenfunctions are prerequisites for applying EEM to the relevant dynamic problems. Orthogonality guarantees that the inner product of eigenfunctions from different modes or families is zero, which allows the analytical solution for transient waveforms to be presented in a concise form; completeness guarantees that any other function in the space spanned by the eigenfunctions can be linearly expanded. For a general application of eigenfunctions, orthogonality can be proven according to the Sturm–Liouville theory (Love, 1944; Stakgold and Holst, 2011). However, completeness is a more severe problem and difficult to prove because of the complexity of mathematics. Gurtin (1984) proved the completeness of the eigenfunctions corresponding to some

elastic problems assuming that only one eigenfunction corresponds to an eigenvalue. Nevertheless, the completeness of eigenfunctions for this study is much more complex since several eigenfunctions correspond to a given eigenvalue. Therefore, the completeness of eigenfunctions in complex waveguides is usually assumed but not strictly proved (Weaver and Pao, 1982; Liu and Qu, 1998; Yin and Yue, 2002; Tang and Wu, 2012; Tang *et al.*, 2012; Zernov *et al.*, 2006). This study also assumed completeness.

A. Eigenfunctions

Denote the set of eigenfunctions as $\{\tilde{\mathbf{u}}_{mn}(\mathbf{x})\}$, each of which is governed by the steady-state problem corresponding to Eq. (3), that is,

$$\mathbf{L}_i[\tilde{\mathbf{u}}_{mn}(\mathbf{x})] + \rho_i \omega_{mn}^2 \tilde{\mathbf{u}}_{mn}(\mathbf{x}) = 0, \quad \text{in } D_i, \quad i = 1, 2, \quad (11)$$

where ω_{mn} is the eigenvalue, n denotes the subscript of the discrete wavenumber, and m denotes the order index of mode corresponding to the n th discrete wavenumber. Solving Eq. (11) with the Helmholtz decomposition method gives the components

$$\begin{aligned} \tilde{u}_{1mn}^r(r, z) &= (A_{1mn} \cos \alpha_{1mn} z + B_{1mn} \sin \alpha_{1mn} z) k_n J_0'(k_n r) \\ &\quad + \beta_{1mn} (-C_{1mn} \sin \beta_{1mn} z \\ &\quad + D_{1mn} \cos \beta_{1mn} z) k_n J_0'(k_n r), \end{aligned} \quad (12)$$

$$\begin{aligned} \tilde{u}_{1mn}^z(r, z) &= \alpha_{1mn} (-A_{1mn} \sin \alpha_{1mn} z + B_{1mn} \cos \alpha_{1mn} z) J_0(k_n r) \\ &\quad + k_n^2 (C_{1mn} \cos \beta_{1mn} z + D_{1mn} \sin \beta_{1mn} z) J_0(k_n r), \end{aligned} \quad (13)$$

$$\tilde{u}_{2mn}^r(r, z) = (A_{2mn} \cos \alpha_{2mn} z + B_{2mn} \sin \alpha_{2mn} z) k_n J_0'(k_n r), \quad (14)$$

$$\tilde{u}_{2mn}^z(r, z) = \alpha_{2mn} (-A_{2mn} \sin \alpha_{2mn} z + B_{2mn} \cos \alpha_{2mn} z) J_0(k_n r), \quad (15)$$

where $A_{1mn}, B_{1mn}, C_{1mn}, D_{1mn}, A_{2mn}$, and B_{2mn} are constants to be determined, k_n is the discrete wavenumber in the r -direction, $\alpha_{1mn} = \sqrt{\omega_{mn}^2/c_{1L}^2 - k_n^2}$ and $\beta_{1mn} = \sqrt{\omega_{mn}^2/c_{1T}^2 - k_n^2}$ are the wavenumber of the longitudinal and transverse waves in ice in the z -direction, respectively, $\alpha_{2mn} = \sqrt{\omega_{mn}^2/c_{2L}^2 - k_n^2}$ is the wavenumber of the longitudinal wave in the water in the z -direction, and J_0 and J_0' are the zeroth-order first-kind Bessel function and its first-order derivative, respectively.

The orthogonal nature of the eigenfunctions is readily proven, details of which can be found for a similar example in Tang and Wu (2012). Taking the density ρ of the medium as the weight, we obtain

$$\sum_{i=1}^2 \int_{D_i} \rho_i \tilde{\mathbf{u}}_{imn} \cdot \tilde{\mathbf{u}}_{ipq} dV = \delta_{mp} \delta_{nq} \gamma_{mn}, \quad (16)$$

where δ_{mp} and δ_{nq} are the Kronecker delta functions and γ_{mn} denotes the modulus of the function family $\{\tilde{\mathbf{u}}_{mn}(\mathbf{x})\}$.

B. Analytical solution

Eringen and Suhubi (1975) presented a standard derivation of applying EEM for a general elastic body with boundaries. In the function space spanned by the eigenfunctions $\{\tilde{\mathbf{u}}_{mn}(\mathbf{x})\}$, the analytical solution of transient displacement of acoustic waves in the composite structure is given by

$$u(\mathbf{x}, t) = \sum_{m,n} \left\{ \frac{1}{\gamma_{mn} \omega_{mn}} \int_0^t \int_D \rho \mathbf{f}(\mathbf{x}, \tau) \cdot \tilde{\mathbf{u}}_{mn}(\mathbf{x}) \sin[\omega_{mn}(t - \tau)] dV d\tau \right\} \tilde{\mathbf{u}}_{mn}(\mathbf{x}). \quad (17)$$

The transient displacement in the ice–water composite structure can be obtained by numerically calculating Eq. (17). Moreover, it should be noted that the analytical solution provided by Eringen and Suhubi (1975) was derived for a single elastic body, while Eq. (17) was developed for solid–liquid coupled system, which would be more complicated.

IV. NUMERICAL CALCULATION

As an example, we consider a scenario in which a cylindrical transducer excites acoustic waves in the water. The force generated by the transducer is assumed to be

$$\mathbf{f}(r, z, t) = F_0 \frac{\delta(r - r_0)}{2\pi\rho_2 r} g(t) \mathbf{e}_r, \quad z_0 - \frac{h_0}{2} \leq z \leq z_0 + \frac{h_0}{2}, \quad (18)$$

where F_0 is the amplitude of the body force, δ is the Dirac function, r_0 and h_0 are the radius and height of the cylindrical transducer, respectively, and $g(t)$ is simulated as an eight-cycle single-frequency sine signal modulated by a Hanning window, which is given by

$$g(t) = \begin{cases} \sin(2\pi f_0 t) \left[0.5 - 0.5 \cos\left(\frac{2\pi f_0 t}{8}\right) \right], & 0 < t < 8/f_0, \\ 0, & \text{else,} \end{cases} \quad (19)$$

where f_0 is the center frequency.

C. Numerical procedure

The numerical procedures for calculating the transient displacement are as follows.

1. Construct and solve the dispersion equation

Rose (1999) summarized a method for constructing a dispersion equation for multilayer composite structures. For the ice–water composite structure shown in Fig. 1, a set of discrete wavenumbers $\{k_n\}_{n=1}^N$ was generated according to the following equation:

$$J'_0(k_n R) = 0, \quad n = 1, 2, \dots, N, \quad (20)$$

where N is the upper bound index of wavenumber. By substituting k_n ($n = 1, 2, \dots, N$) into Eqs. (7)–(9), the dispersion equation was derived from a system of linear equations of eigen displacement coefficients $A_{1mn}, B_{1mn}, C_{1mn}, D_{1mn}, A_{2mn}$, and B_{2mn} in Eqs. (12)–(15), which is an implicit function consisting of the eigenvalue ω_{mn} and wavenumber k_n , that is,

$$\mathbf{A}\mathbf{y} = 0, \quad (21)$$

where $\mathbf{y} = [A_{1mn} B_{1mn} C_{1mn} D_{1mn} A_{2mn} B_{2mn}]^T$ is a column vector, the superscript T represents the transpose of the matrix, and \mathbf{A} is a sixth-order square matrix (Liu *et al.*, 2021). The equivalent condition for Eq. (21) to have a non-trivial solution is

$$\det(\mathbf{A}) = 0. \quad (22)$$

Equation (22) is the dispersion equation for a wave propagating in the ice–water composite structure.

It should be noted that although there were infinite eigenvalues that were associated with a given wavenumber, only finite modes would be excited under a specific external force. Denote the maximum mode index of eigen circle frequency as M , i.e., for a given wavenumber k_n , the first M orders eigen circle frequencies ω_{mn} ($m = 1, 2, \dots, M$) are required. The bisection method was used to solve Eq. (22) since it is the easiest to implement numerically.

2. Calculate parameters based on the dispersion relationship

The eigen displacement coefficients were obtained according to the following Newton–Raphson iterative scheme:

$$\mathbf{y}^{(s+1)} = \mathbf{y}^{(s)} - \mathbf{J}^{-1}(\mathbf{y}^{(s)}) \boldsymbol{\eta}(\mathbf{y}^{(s)}), \quad (23)$$

where $\mathbf{y}^{(s)} = [A_{1mn}^{(s)} B_{1mn}^{(s)} C_{1mn}^{(s)} D_{1mn}^{(s)} A_{2mn}^{(s)} B_{2mn}^{(s)}]^T$ corresponds to (k_n, ω_{mn}) , s is the iterative index, and $\boldsymbol{\eta}$ is a six-order vector with the following elements:

$$\eta_p(\mathbf{y}^{(s)}) = \begin{cases} \sum_{q=1}^6 [y_q^{(s)}]^2 - 1, & p = 1, \\ \sum_{q=1}^6 M_{pq} y_q^{(s)}, & p = 2, 3, \dots, 6, \end{cases} \quad (24)$$

where M_{pq} is component of the coefficient matrix corresponding to the dispersion equation (Liu *et al.*, 2021), and \mathbf{J}^{-1} is the inversed Jacobian matrix corresponding to $\boldsymbol{\eta}$, i.e.,

$$\mathbf{J}^{-1}(\mathbf{y}^{(s)}) = \text{inv} \left[\frac{\partial(\eta_1, \dots, \eta_6)}{\partial(y_1^{(s)}, \dots, y_6^{(s)})} \right]. \quad (25)$$

Furthermore, the modulus γ_{mn} of eigenfunctions was calculated by Eq. (16) when $m = p$ and $n = q$.

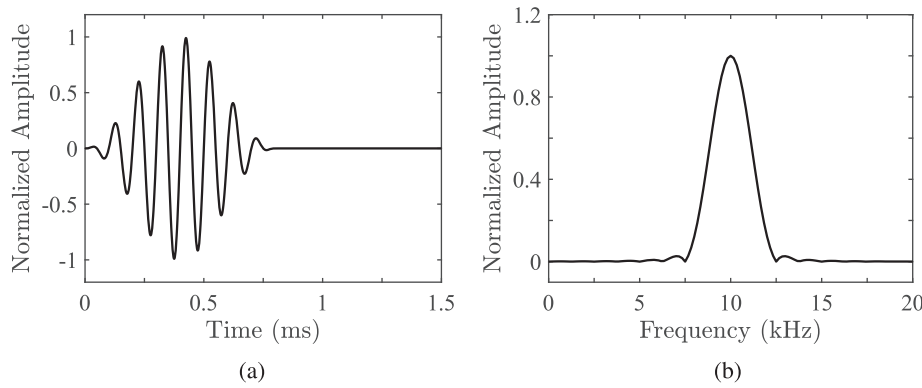


FIG. 2. The (a) time-domain waveform and (b) frequency spectrum of signal $g(t)$ with center frequency $f_0 = 10$ kHz.

3. Calculate the transient displacement

With eigen displacement coefficients and required parameters, the transient displacement for the m th order mode was calculated by

$$\mathbf{u}_m(r, z, t) = \sum_{n=1}^N \left\{ \frac{F_0}{\gamma_{mn} \omega_{mn}} \int_{z_0-h_0/2}^{z_0+h_0/2} \tilde{u}_{2mn}^r(r_0, z) dz \times \int_0^t g(\tau) \sin[\omega_{mn}(t-\tau)] d\tau \right\} \tilde{\mathbf{u}}_{mn}(r, z), \quad (26)$$

and the total transient displacement was obtained by superposing all excited modes, i.e.,

$$\mathbf{u}(r, z, t) = \sum_{m=1}^M \mathbf{u}_m(r, z, t). \quad (27)$$

D. Verification

To validate the theoretical derivation and numerical code, the transient waveforms calculated using EEM were compared with those simulated using the finite element method (FEM). Without loss of generality, a small-scaled ice–water composite structure was used. The depths of the ice and water for the composite structure were 0.1 and 0.2 m, respectively. The following parameters were used in the calculations (McCammon and McDaniel, 1985): The longitudinal and transverse wave velocities in the ice were 3593.4 and 1809.8 m/s, respectively. The wave velocity in the water was 1500 m/s. Moreover, the densities of the ice and water were 917 and 1000 kg/m³, respectively.

The outer radius, height, and vertical position of the cylindrical transducer were 0.05, 0.001, and 0.1 m, respectively. The center frequency f_0 and amplitude F_0 for the excitation pulse signal were 10 kHz and 10^8 N/m³, respectively. The acoustic parameters of the ice and water were unchanged for subsequent calculations.

As shown in Fig. 2(b), the energy of the signal $g(t)$ defined by Eq. (19) with a center frequency of 10 kHz concentrated in the frequency range of 7.5–12.5 kHz. Therefore, modes with cutoff frequencies greater than 12.5 kHz were ignored when using Eq. (27) to calculate the total transient

displacement. Figure 3 shows the group-velocity dispersion curves of the first ten modes in the small-scaled ice–water composite structure. All higher-order (greater than second-order) modes had cutoff frequencies; moreover, the cutoff frequency increased with mode order. The cutoff frequency of the eighth-order mode was approximately 14.3 kHz, meaning that external forces in the frequency range of 7.5–12.5 kHz could only excite the first seven modes of guided waves. Consequently, these seven modes were superposed to calculate the total transient displacement.

Figure 4 shows the radial and axial transient displacements of the first seven modes when the receiving point was located at $r = 1$ m on the upper surface of the ice, which were calculated using Eq. (26). Figure 4 shows that the fourth-order mode has the largest amplitude in both directions; therefore, it is the largest contributor to the total waveform. It should be noted that the excitation efficiency of different modes depends on the geometrical and material parameters of the composite structure and the properties of the external force.

The total radial and axial transient displacement waveforms were obtained by superposing the radial and axial displacements of the first seven modes directly, respectively. The total radial and axial displacements of the receiving point located at $r = 1$ m on the upper surface of the ice layer are presented in Fig. 5. The blue dot lines and red solid lines in Fig. 5 correspond to the results calculated using EEM and FEM, respectively. The two methods agree, which indicates

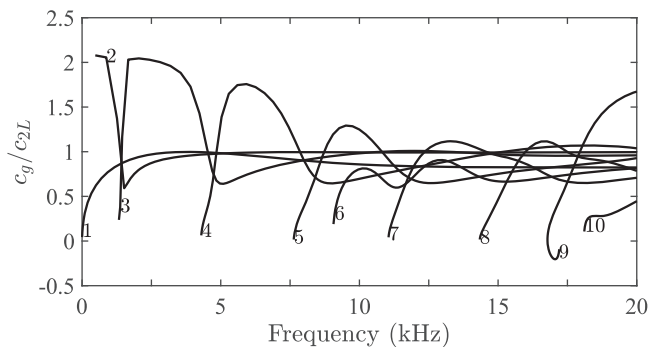


FIG. 3. Group-velocity c_g dispersion curves of the first ten modes in the small-scaled ice–water composite structure. c_{2L} represents the longitudinal wave velocity in the water used to normalize group-velocity. The numbers near the curves denote the mode indices.

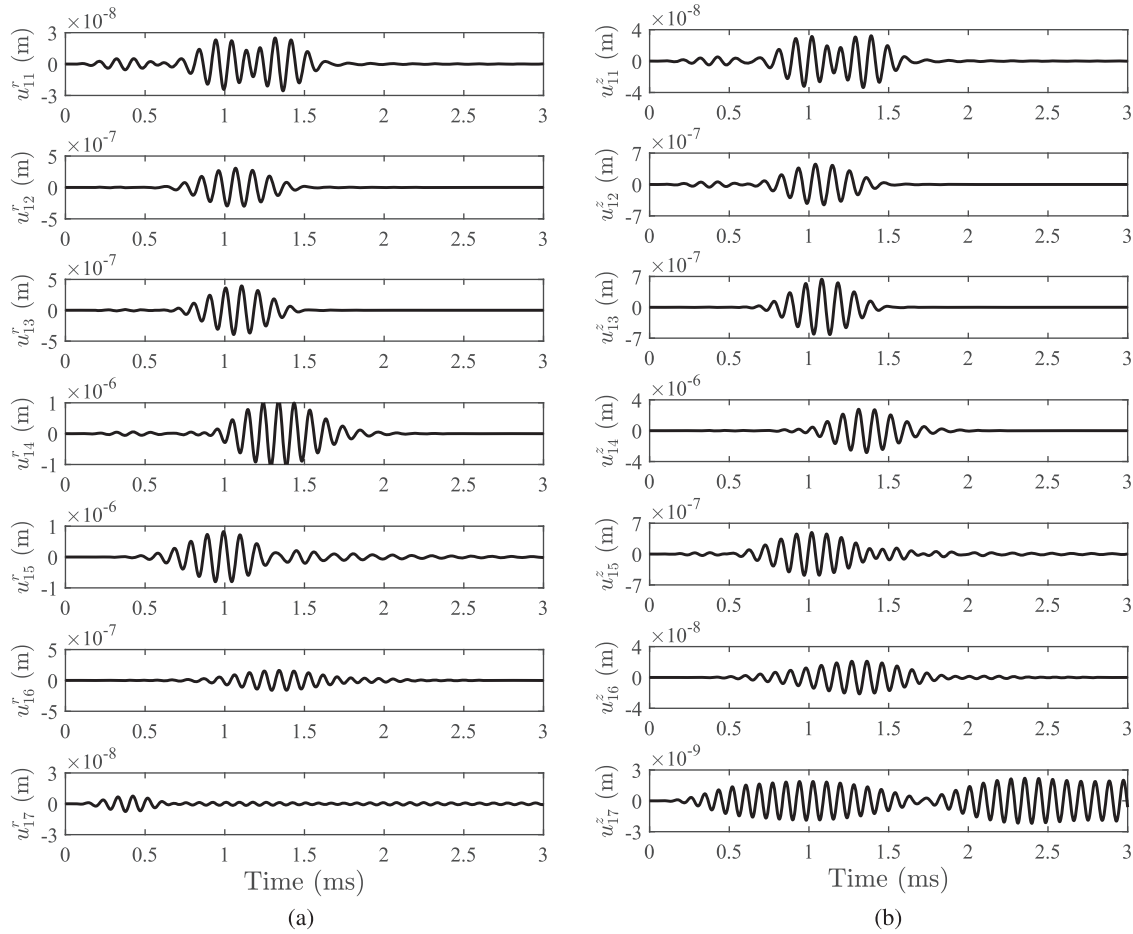


FIG. 4. Radial (a) and axial (b) transient displacements of the first seven modes at a receiving point located at $r = 1$ m on the upper surface of the ice in a small-scaled composite structure. Waveforms in both directions with the same magnitude are presented in the same scaled vertical axis.

that the theoretical derivation and numerical procedure are correct and the prior assumption of completeness is reasonable. In the radial direction, the total waveform exhibits two packets, which are mainly contributed from the fourth- and fifth-order mode in this direction, i.e., u_{14}^r and u_{15}^r in Fig. 4(a). In the axial direction, it seems to be only one packet, which mainly comes from the fourth-order mode because it has far higher magnitude over other modes; however, it should be noted that the third- and fifth-order modes in the axial direction also contribute to this packet, which exhibits

the combination characteristics of the third- and fifth-order modes near 1 ms, as shown in Figs. 4(b) and 5(b).

Although total transient displacements of the ice–water composite structure can be obtained by either EEM or FEM, the former has the following advantages. (i) The calculation efficiency of EEM is much higher than that of FEM (Liu and Qu, 1998; Tang and Xu, 2010). In the same computational environment (Intel Core i7-7700, 3.6 GHz, 16 GB RAM; Intel, Santa Clara, CA), FEM cost 18 min to obtain the numerical results shown in Fig. 5, while EEM cost only

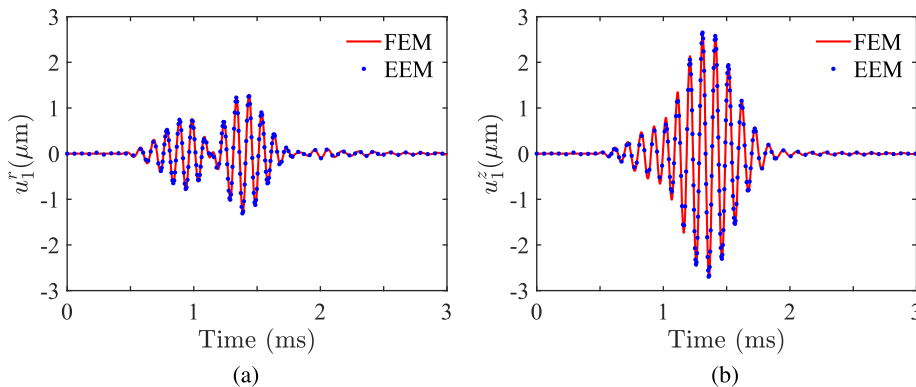


FIG. 5. (Color online) Total radial (a) and axial (b) displacements of the receiving point located at $r = 1$ m on the upper surface of the ice. Transient waveforms simulated by the FEM are plotted with red solid lines and calculated by the EEM are plotted with blue dot lines.

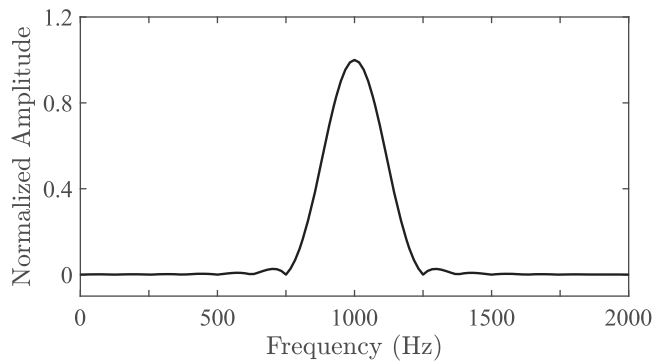


FIG. 6. Spectrum distribution of signal $g(t)$ with a center frequency of 1 kHz.

7 min. The gap in computation time between FEM and EEM will increase dramatically as the scale of the structure increases (Collins *et al.*, 2019; He *et al.*, 2023). (ii) The displacement corresponding to each mode can be calculated separately using EEM; thus, the excitation efficiency and propagation characteristics of each mode can be quantitatively analyzed (Tang and Wu, 2012). These advantages are significant when analyzing transient acoustic wave propagation in the Arctic Ocean. Note that it is almost impossible to fulfill this task using FEM owing to the large scale of the ocean.

E. Numerical results and discussions

Here, we use the trans-ice propagation characteristics of acoustic waves in the Arctic Ocean with a sea depth of 100 m as an example. The following parameters were used in the calculation. $R = 4000$ m; the center position z_0 , outer radius r_0 , and height h_0 of the cylindrical transducer were 2.1, 0.4, and 0.2 m, respectively. The center frequency and amplitude of the external force were 1000 Hz and 10^8 N/m³, respectively. As shown in Fig. 6, the energy of the signal $g(t)$ defined by Eq. (19) with frequency $f_0 = 1000$ Hz is mostly distributed within the frequency range of 750–1250 Hz.

Figure 7 shows the group-velocity dispersion curves within the frequency range of 700–1300 Hz with an ice thickness of 2 m. The cutoff frequencies of the 173rd and higher-order modes were greater than 1250 Hz, whereas those of the 172nd and lower modes were less than 1250 Hz.

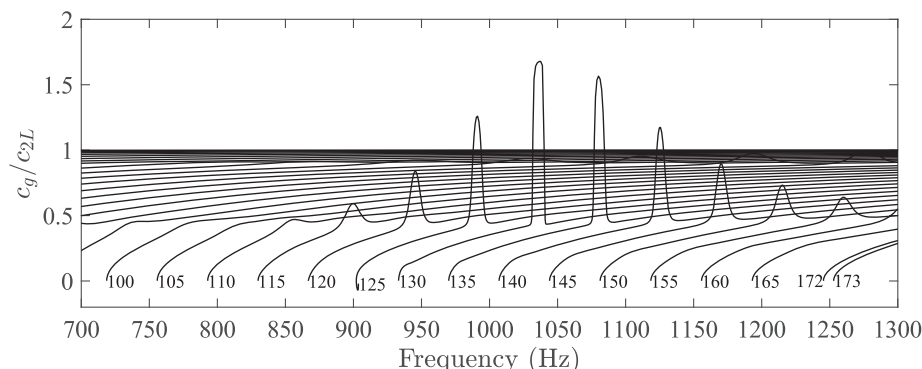


FIG. 7. Group-velocity c_g dispersion curves within the frequency range of 700–1300 Hz with an ice thickness of 2 m. c_{2L} represents the longitudinal wave velocity in the water used to normalize group-velocity. The numbers near the curves denote the mode indices.

Therefore, only the first 172 modes were required to calculate the total displacement in this scenario. Within the frequency range of 750–1250 Hz, the group-velocity increased with an increase in frequency and approached the acoustic velocity of the water when the mode order was less than 110, whereas the group-velocity presented a maximum when the mode order was equal to or greater than 110. The frequency corresponding to the maximum moves toward higher frequencies with increasing mode order. The maximum group-velocity of the 130th mode was approximately 2517 m/s, which is much greater than the acoustic velocity of the water.

1. Excitation source in the water layer

Figure 8 shows the transient radial and axial displacements at $r = 50$ m. Figures 8(a) and 8(b) show the displacement waveforms received on the upper surface of the ice. Figures 8(c) and 8(d) show the displacement waveforms received in water with a depth $z = 6$ m. The amplitude of the radial displacement on the upper surface of the ice was much smaller than that in water, whereas the amplitude of the axial displacement on the upper surface of the ice was slightly greater than that in water, as shown in Fig. 8. The radial displacement on the upper surface of the ice exhibited noticeable dispersion characteristics. Its waveform consisted primarily of three wave packets, P_1 , P_2 , and P_3 in Fig. 8(a). Moreover, the amplitudes of the first and second wave packets were significantly smaller than those of the third main wave packet. The propagation velocities of the first and second wave packets were approximately $1.6 c_{2L}$ and $1.3 c_{2L}$, respectively, which were close to the group-velocities of the 125th and 140th modes, respectively, as shown in Fig. 7. The propagation velocity of the third wave packet was approximately c_{2L} . The dispersion characteristics of the axial displacement on the upper surface of the ice are not obvious, as are the radial and axial displacements in water. Their waveforms consisted primarily of a single wave packet.

Figure 9 shows the transient radial and axial displacements on the upper surface of the ice at $r = 75$ and 100 m. Comparing Figs. 9 and 8, we can see that the amplitudes of the radial and axial displacements decrease sharply with increasing distance, and their propagation loss is greater than 6 dB per doubling of distance. Moreover, it can be seen

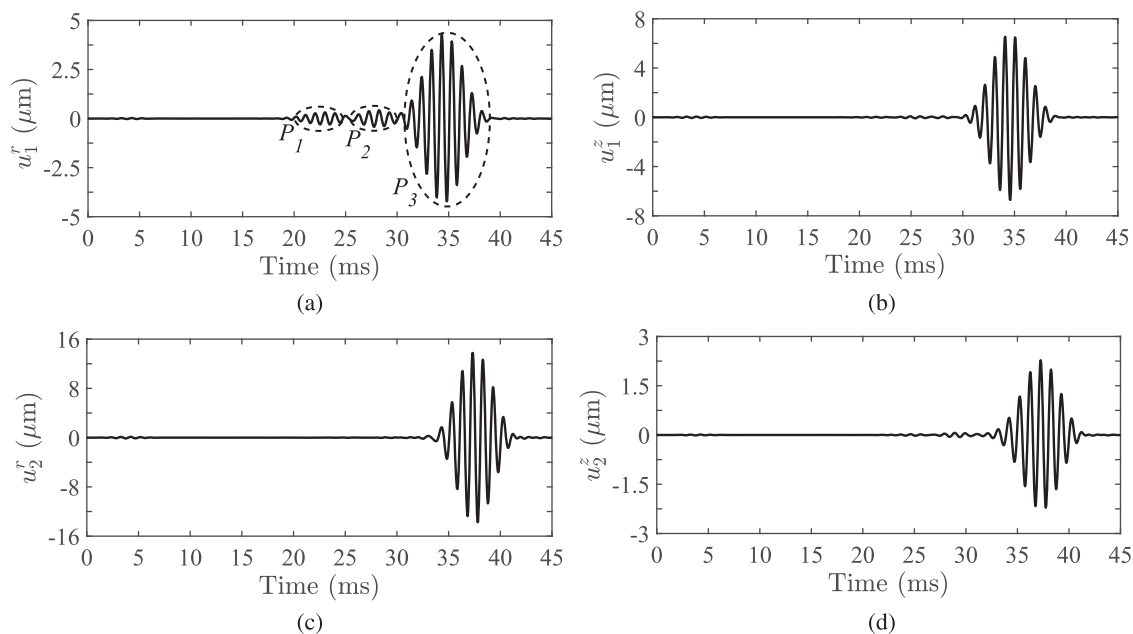


FIG. 8. Transient displacements at $r = 50$ m. (a) Radial, and (b) axial displacement on the upper surface of the ice; (c) radial, and (d) axial displacement in the water at a depth $z = 6$ m.

from Figs. 8(a) and 9(a) and 9(c) that the relative time gap between the two small wave packets and the main wave packet becomes longer, further indicating that the main packet consists of lower-order modes with a lower group-velocity, while the two small packets consist of higher-order modes with a higher group-velocity. It should be noted that the waveform shape of the radial displacement depends largely on distance, and the relative amplitude of the first two packets to the third increases with increasing distance. This result shows a much more evident dispersion characteristic for the radial

displacement, and its waveform is distorted more severely as the propagating distance increases.

A frequency spectra distribution comparison of excitation $g(t)$ and transient waveforms shown in Figs. 8 and 9 are presented in Fig. 10. The frequency-selective fading occurred owing to the influence of the dispersion characteristics, especially evident in the radial direction, as shown in Fig. 10(a).

The ice thickness of the Arctic varies with the climate, season, and hydrographic conditions of the sea. Its effect on

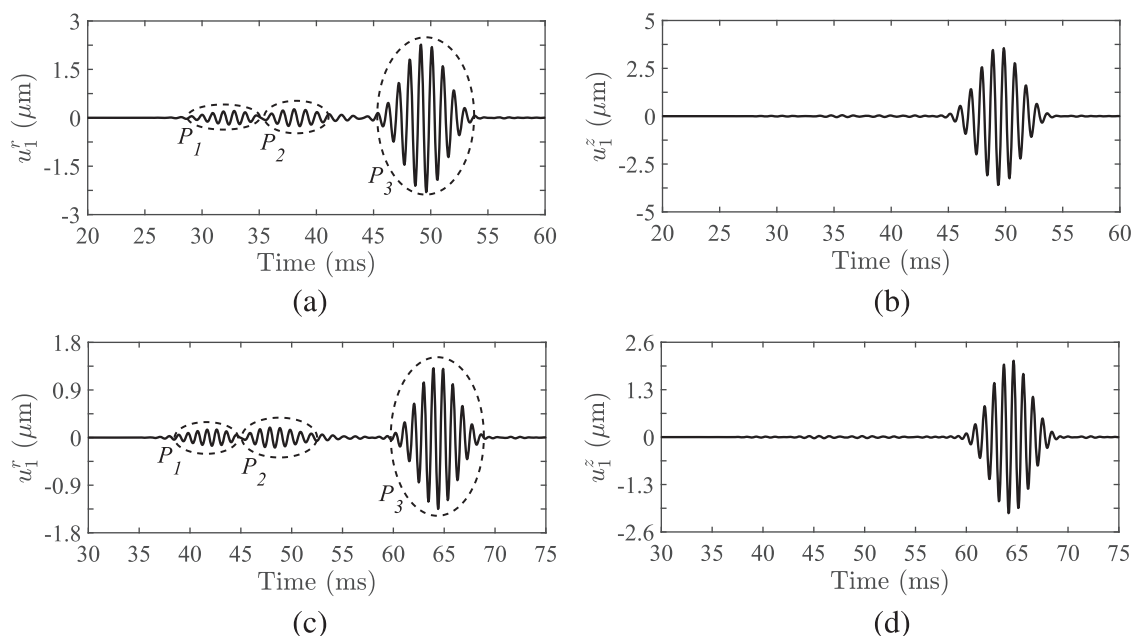


FIG. 9. Transient displacements on the upper surface of the ice layer for different propagation distances. (a) Radial and (b) axial displacement at a distance of $r = 75$ m; (c) radial and (d) axial displacement at a distance of $r = 100$ m.

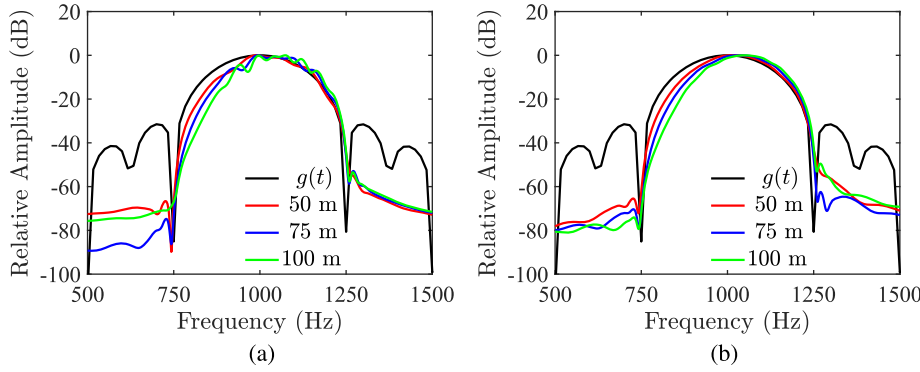


FIG. 10. (Color online) Frequency spectra of the transient (a) radial and (b) axial displacements for different propagation distances.

the dispersion characteristics of waves in the ice–water composite structures has been previously investigated (Liu *et al.*, 2021). Figure 11 shows the transient displacements on the surface of the ice for different thicknesses. The ice thicknesses used in the calculations of Figs. 11(a) and 11(b) were 4 m, and those corresponding to Figs. 11(c) and 11(d) were 6 m, which represents the typical mean thickness of ice in the Arctic (Haas *et al.*, 2010). Thicker ice results in a shift of group-velocity dispersion curves to a lower frequency; therefore, for a given external excitation, more guided wave modes need to be superposed when calculating the transient waveforms using Eq. (27). For an ice layer with 4 m, 176 modes were superposed, and for 6 m, 181 modes were needed. Comparing Figs. 11 and 8, the ice thickness has a significant impact on both displacements, especially on radial displacements. In general, the thicker the ice, the greater the waveform distortion. It should be noted that the ice absorption loss was ignored in this study.

Figure 12 shows the frequency spectra distribution of the radial and axial displacements on the upper surface of the ice layer with different ice thicknesses. The ice thickness

has a significant influence on the spectra of both directions. Moreover, the radial displacement exhibited more evident frequency-selective fading as the thickness of the ice layer increased. Therefore, better performance may be achieved by using the axial information for trans-ice acoustic communication.

2. Excitation source on the upper surface of the ice

As another application of trans-ice communication, we considered a scenario in which the excitation source was a disk transducer placed on the upper surface of the ice layer, exciting acoustic waves vertically downwards. The receivers were located 50 m from the source. The radius of the disk transducer was $r_0 = 0.2$ m, and the center frequency and amplitude of the external force were 1 kHz and 10^8 N/m³, respectively. Accordingly, Eq. (18) must be adjusted as follows:

$$\mathbf{f}(r, z, t) = F_0 \frac{\delta(z + h_1)}{\rho_1} g(t) \mathbf{e}_z, \quad 0 \leq r \leq r_0. \quad (28)$$

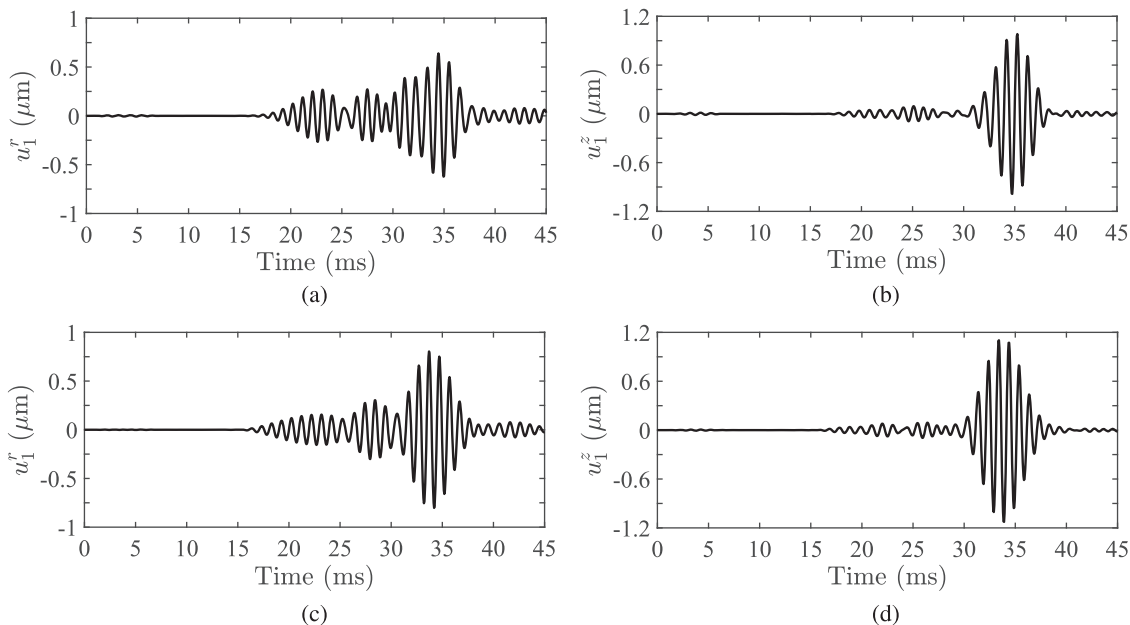


FIG. 11. Transient displacements on the upper surface of the ice for different ice thicknesses. (a) Radial and (b) axial displacement for an ice thickness of 4 m, and (c) radial and (d) axial displacement for an ice thickness of 6 m.

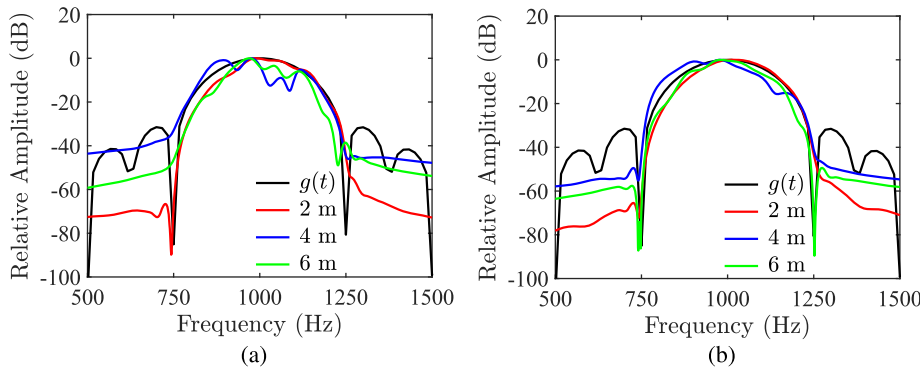


FIG. 12. (Color online) Frequency spectra of the transient displacements on the upper surface of the ice for different ice thicknesses. (a) Radial and (b) axial displacement.

The transient displacements were calculated according to the numerical procedures described in Sec. IV A. The numerical results are shown in Fig. 13. The depths of the ice and water were 2 and 100 m, respectively. Comparing Figs. 8 and 13, there is no significant difference between the waveforms of the received transient guided waves when the transducer was placed on the upper surface of the ice layer or in the water, except for a slight distortion in the axial displacement at the receiving point in the water layer. The radial displacement at the receiver on the ice consisted of three wave packets, that is, P_1 , P_2 and P_3 , as shown in Fig. 13(a). The propagation time of the transient guided wave in the water layer was slightly shorter when the excitation was located on the surface of the ice, as shown in Figs. 8(c) and 8(d), and 13(c) and 13(d). One factor contributing to this phenomenon is the difference in acoustic speed between ice and water; both the transverse and longitudinal speeds in the ice layer are greater than the longitudinal speed in the water.

However, a general pattern on the amplitude of transient waveforms can be obtained by summarizing Figs. 8, 9, 11, and 13, that is, the radial displacement of the receiver on the surface of the ice is always smaller than the axial

displacement, regardless of whether the excitation source is on the ice or in the water, whereas this relationship is reversed for a receiver in the water layer.

Figure 14 presents the frequency spectra distributions of the transient waveforms shown in Figs. 8(a) and 8(b), and 13(c) and 13(d). The frequency-selective fading characteristics of the signal are related to the location of the excitation and the direction of the vector displacement. It can be concluded from the spectra in Figs. 10, 12, and 14 that, if we want to conduct trans-ice acoustic communication, using axial displacements received in water or radial displacements received on ice may be more productive than the other way around because there are weak distortions in these directions. Therefore, the application scenario determines where the excitation and receiving points should be placed and which direction should be adopted.

V. CONCLUSION

To analyze transient acoustic wave propagation across the ice layer in the Arctic Ocean, an ice–water composite structure was developed. An analytical solution for transient

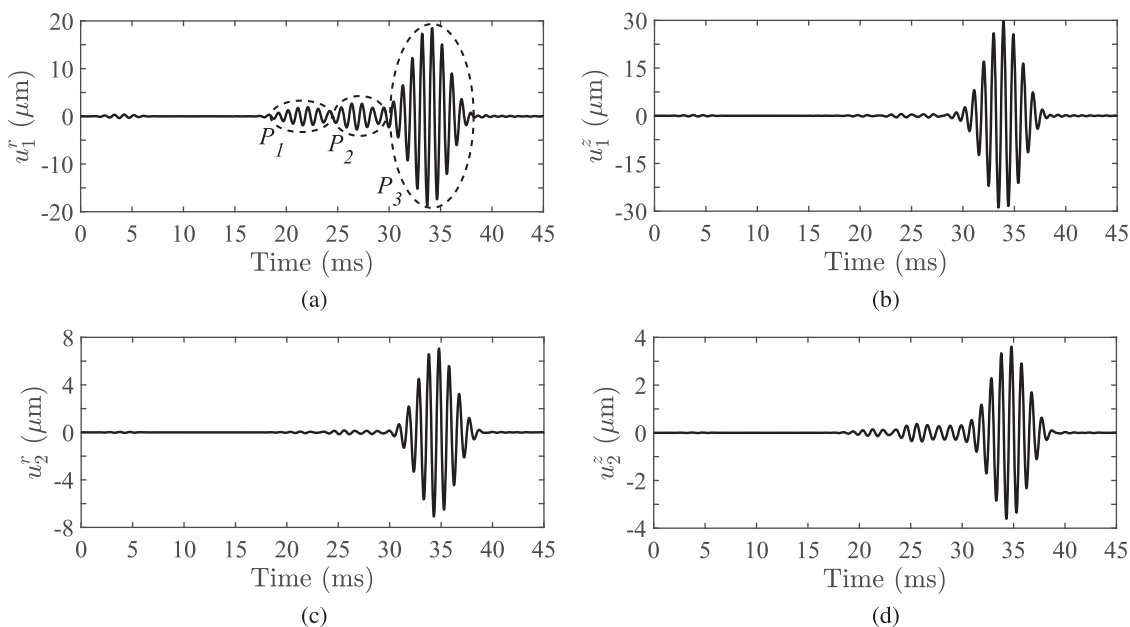


FIG. 13. Transient displacements at $r = 50$ m with an excitation source on the upper surface of the ice. (a) Radial and (b) axial displacement on the upper surface of the ice, and (c) radial and (d) axial displacement in the water at depth $z = 2$ m.

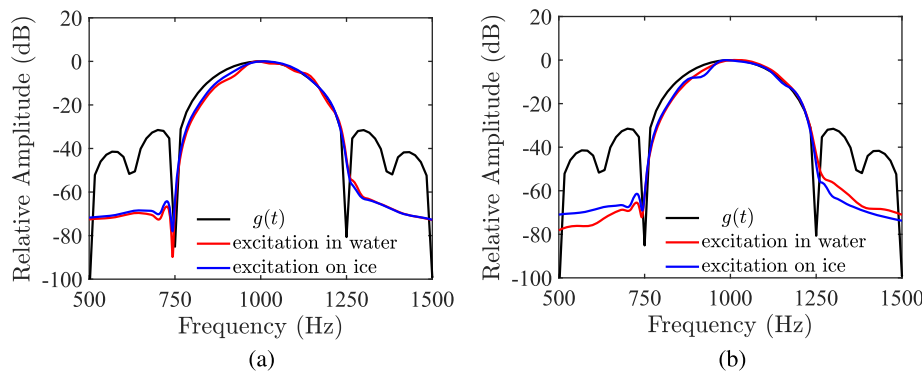


FIG. 14. (Color online) Frequency spectra of the transient (a) radial and (b) axial displacements when the excitation source is placed on the surface of the ice and in the water.

displacement in the structure was derived using EEM. Moreover, numerical procedures for calculating the transient displacement were proposed. The radial and axial displacements and frequency spectra were numerically analyzed.

The numerical results showed that the waveform of the radial displacement was much more complicated than that of the axial displacement. The amplitudes of both radial and axial displacements decreased rapidly with increasing propagation distance. The propagation losses were greater than 6 dB per doubling of distance. Ice thickness was shown to have a significant impact on the amplitudes and waveforms of the radial and axial displacements. Generally, the thicker the ice, the more complicated the waveform and the greater the distortion. Moreover, the amplitudes of the axial displacements received on the surface of the ice are always greater than the radial displacements, whereas, in the water layer, the amplitudes of the radial displacements are always greater than the axial displacements, regardless of the position of the acoustic source.

The frequency spectra of the transient radial and axial displacements exhibited frequency-selective fading owing to dispersion characteristics. When the excitation source was placed in the water, the frequency-selective fading corresponding to the radial displacement was more severe than that corresponding to the axial displacement. In general, radial waveforms exhibit more noticeable distortions. Therefore, utilizing axial displacement information and generating signals in the water to perform trans-ice communication may be better than using radial information. However, using radial displacement information may be a good choice for other applications, such as the inversion of ice thickness and measurement of acoustic parameters.

Compared to the reflectivity method (Muller, 1985), the transfer matrix method (Sastry and Munjal, 1998; Yue and Yin, 1998), and FEM, EEM has advantages in investigating the transient response of large-scaled ice–water composite structures for the Arctic Ocean. Each guided wave mode can be evaluated separately using EEM, which provides a guideline for the excitation control of guided waves. Distributions fields of displacement and stress can be efficiently obtained by EEM. Further, the numerical program in this paper can be generalized to the investigation of ice-covered deep-sea propagation, where more modes need to be superposed and the acoustic velocity profile should be taken into

consideration. Experimental tests will be conducted to verify the EEM for the frozen Arctic Ocean proposed in this paper.

ACKNOWLEDGMENTS

This work was supported by the National Natural Science Foundation of China (U22A2012), and the Open Fund of State Key Laboratory of Acoustics, Chinese Academy of Sciences (SKLA202101, SKLA202309).

AUTHOR DECLARATIONS

Conflict of Interest

No potential conflict of interest was reported by the authors.

DATA AVAILABILITY

Data sharing is not applicable to this article as no new data were created or analyzed in this study.

- Alexander, P., Duncan, A., Bose, N., and Smith, D. (2013). "Modelling acoustic transmission loss due to sea ice cover," *Acoust. Aust* **41**(1), 79–86, available at <http://hdl.handle.net/20.500.11937/2321>.
- Burke, J. E., and Twersky, V. (1966). "Scattering and reflection by elliptically striated surfaces," *J. Acoust. Soc. Am.* **40**(4), 883–895.
- Chen, W., Hu, S., Wang, Y., Yin, J., Korochensev, V. I., and Zhang, Y. (2021). "Study on acoustic reflection characteristics of layered sea ice based on boundary condition method," *Waves Random Complex Media* **31**(6), 2177–2196.
- Collins, M. D., and Siegmund, W. L. (2021). "Parabolic equation techniques for seismology, seismo-acoustics, and arctic acoustics," *J. Theor. Comput. Acoust.* **29**(2), 2130003.
- Collins, M. D., Turgut, A., Menis, R., and Schindall, J. A. (2019). "Acoustic recordings and modeling under seasonally varying sea ice," *Sci. Rep.* **9**(1), 8323.
- Diachok, O. I. (1976). "Effects of sea-ice ridges on sound propagation in the Arctic Ocean," *J. Acoust. Soc. Am.* **59**(5), 1110–1120.
- Dosso, S. E. (2014). "Three-dimensional localization of transient acoustic sources using an ice-mounted geophone," *J. Acoust. Soc. Am.* **135**(1), 124–133.
- Dosso, S. E., Heard, G. J., and Vinnins, M. (2002). "Source bearing estimation in the Arctic Ocean using ice-mounted geophones," *J. Acoust. Soc. Am.* **112**(6), 2721–2734.
- Dosso, S. E., Vinnins, M., and Heard, G. J. (2003). "Arctic field trials of source bearing estimation using ice-mounted geophones (L)," *J. Acoust. Soc. Am.* **113**(6), 2980–2983.
- Eringen, A. C., and Suhubi, E. S. (1975). *Elastodynamics* (Academic Press, New York), Vol. II, pp. 437–442.
- Gavrilov, A. N., and Mikhalevsky, P. N. (2006). "Low-frequency acoustic propagation loss in the Arctic Ocean: Results of the Arctic climate

- observations using underwater sound experiment," *J. Acoust. Soc. Am.* **119**(6), 3694–3706.
- Gurtin, M. E. (1984). *The Linear Theory of Elasticity* (Springer-Verlag, Berlin), Vol. II, pp. 270–272.
- Haas, C., Hendricks, S., Eicken, H., and Herber, A. (2010). "Synoptic airborne thickness surveys reveal state of Arctic sea ice cover," *Geophys. Res. Lett.* **37**, L09501, <https://doi.org/10.1029/2010GL042652>.
- Han, X., Yin, J. W., Chen, W., and Ge, W. (2019). "Cross-ice acoustic communication by ice-mounted geophones: An initial experimental demonstration," *Appl. Acoust.* **150**, 302–306.
- He, T., Wang, B., Tang, S., Zhou, F., Mo, S., and Fang, E. (2023). "Numerical simulation of wave propagation in ice-covered ocean environments based on the equivalent-source method," *Phys. Fluids*, **35**, 047126.
- Hope, G., Sagen, H., Storheim, E., Hobaek, H., and Freitag, L. (2017). "Measured and modeled acoustic propagation underneath the rough Arctic sea-ice," *J. Acoust. Soc. Am.* **142**(3), 1619–1633.
- Kutschale, H. (1969). "Arctic hydroacoustics," *Arctic* **22**(3), 246–264.
- Li, S., Yuan, S., Liu, S., Wen, J., Huang, Q., and Zhang, Z. (2021). "Characteristics of low-frequency acoustic wave propagation in ice-covered shallow water environment," *Appl. Sci.* **11**(17), 7815.
- Liu, G., and Qu, J. (1998). "Transient wave propagation in a circular annulus subjected to transient excitation on its outer surface," *J. Acoust. Soc. Am.* **104**(3), 1210–1220.
- Liu, S. X., Tang, L. G., and Li, Z. L. (2021). "Propagation of acoustic waves in a coupled ice-water system for the Arctic Ocean," *Chin. J. Acoust.* **40**(3), 329–344.
- Love, A. E. H. (1944). *A Treatise on the Mathematics Theory of Elasticity* (Courier Corporation, Chelmsford, MA), 127 pp.
- McCammon, D. F., and McDaniel, S. T. (1985). "The influence of the physical properties of ice on reflectivity," *J. Acoust. Soc. Am.* **77**(2), 499–507.
- Muller, G. (1985). "The reflectivity method: A tutorial," *J. Geophys.* **58**(1), 153–174, available at <https://n2t.net/ark:/88439/y040102>.
- Penhale, M. B., Barnard, A. R., and Shuchman, R. (2018). "Multi-modal and short-range transmission loss in thin, ice-covered, near-shore Arctic waters," *J. Acoust. Soc. Am.* **143**(5), 3126–3137.
- Reeder, D. B., Joseph, J. E., Hill, A. M., and Ainslie, K. N. (2022). "Walking on snow-covered Arctic sea ice to infer ice thickness," *J. Acoust. Soc. Am.* **152**(6), 3809–3818.
- Reismann, H. (1968). "On the forced motion of elastic solids," *Appl. Sci. Res.* **18**, 156–165.
- Reismann, H., and Pawlik, P. S. (1974). "The nonhomogeneous elastodynamics problem," *J. Eng. Math.* **8**(2), 157–165.
- Rose, J. L. (1999). *Ultrasonic Waves in Solid Media* (Cambridge University Press, New York), Chap. 13.
- Sastry, J. S., and Munjal, M. L. (1998). "Response of a multi-layered infinite cylinder to a plane wave excitation by means of transfer matrices," *J. Sound Vib.* **209**(1), 99–121.
- Stakgold, I., and Holst, M. J. (2011). *Green's Functions and Boundary Value Problems* (John Wiley & Sons, New York).
- Tang, L., and Wu, Z. (2012). "Elastodynamic response of bonded solids using the method of eigenfunction expansion," *J. Eng. Math.* **74**, 101–118.
- Tang, L., Wu, Z., Liu, S., and Yang, W. (2012). "Three-dimensional analytical solution for transient guided wave propagation in liquid-filled pipe systems," *IEEE Trans. Ultrason. Ferroelectr. Freq. Control* **59**(8), 1759–1773.
- Tang, L. G., and Xu, X. M. (2010). "Transient torsional vibration responses of finite, semi-infinite and infinite hollow cylinders," *J. Sound Vib.* **329**(8), 1089–1100.
- Weaver, R. L., and Pao, Y. H. (1982). "Axisymmetric elastic waves excited by a point source in a plate," *J. Appl. Mech.* **49**, 821–836.
- Yin, J., Men, W., Zhu, G., and Han, X. (2021). "Experimental study of cross-ice acoustic signal propagation," *Appl. Acoust.* **172**, 107612.
- Yin, X. C., and Yue, Z. Q. (2002). "Transient plane-strain response of multilayered elastic cylinders to axisymmetric impulse," *J. Appl. Mech.* **69**(6), 825–835.
- Yue, Z. Q., and Yin, J. H. (1998). "Backward transfer-matrix method for elastic analysis of layered solids with imperfect bonding," *J. Elast.* **50**, 109–128.
- Zemov, V., Pichugin, A. V., and Kaplunov, J. (2006). "Eigenvalue of a semi-infinite elastic strip," *Proc. R. Soc. A* **462**(2068), 1255–1270.